# Black hole binary inspiral: Analysis of the plunge

Richard H. Price, Sourabh Nampalliwar, and Gaurav Khanna

Phys. Rev. D **93**, 044060 — Published 23 February 2016

DOI: 10.1103/PhysRevD.93.044060

# Black hole binary inspiral: Analysis of the plunge

Richard H. Price
*Department of Physics & Astronomy, and Center for Advanced Radio Astronomy, University of Texas at Brownsville, Brownsville TX 78520*

Sourabh Nampalliwar
*Department of Physics & Astronomy University of Texas at Brownsville, Brownsville TX 78520*

Gaurav Khanna
*Department of Physics, University of Massachusetts, Dartmouth, MA 02747*

Binary black hole coalescence has its peak of gravitational wave generation during the "plunge," the transition from quasicircular early motion to late quasinormal ringing. Although advances in numerical relativity have provided plunge waveforms, there is still no intuitive or phenomenological understanding of plunge comparable to that of the early and late stages. Here we make progress in developing such understanding by relying on insights of the linear mathematics of the particle perturbation model for the extreme mass limit. Our analysis, based on the Fourier domain Green function, and a simple initial model, point to the crucial role played by the kinematics near the "light ring" (the circular photon orbit) in determining the plunge radiation and the excitation of QNR. That insight is then shown to successfully explain results obtained for particle motion in a Schwarzschild background.

## I. OVERVIEW

### A. Background

Interest in the coalescence of binary compact objects was motivated by the development of gravitational wave (GW) detectors, and the need for a better understanding of the endpoint of binary merger[1]. Especially in the case that such mergers end in black hole formation these might be the most powerful, and certainly the most interesting sources of detectible GWs. Beyond that main motivation, there are several other reasons such mergers are of interest to the physics research community; see Ref.[2] for a detailed review. From the outset it was understood[3] that binary coalescence, driven by GW radiation, could be viewed as having three stages. The first is the gradual inspiral of the objects in orbits, most probably nearly circular orbits, gradually decreasing in orbital energy, and hence in radius, driven by the radiation reaction to the GWs being emitted. This first stage can be understood as a quasi-Newtonian process with GW radiation reaction treated as a time averaged loss of orbital energy. Considerable accuracy could be achieved by using post-Newtonian (slow motion, weak field) approximations[4].

The last stage of binary coalescence is the oscillation of the black hole formed by the coalescence. These oscillations, after initial transients, are the "quasinormal ringing" (QNR) of the final hole. It has been known since the early 1970s[5] that these QNRs constitute a spectrum of complex (i.e., damped) frequencies characteristic of the mass and spin of the final black hole.

The second stage, the middle stage in the binary coalescence, may usefully be called the "plunge." It is the end of the early gradual inspiral, and determines the magnitude and phase of the QNR. Most important, this relatively short transition is the stage during which the major part of the GW energy is radiated[6]. Ironically, this most-important stage is the part of the coalescence that is least understood.

For a wide variety of merger scenarios, the excitation of QNR *is* known. The remarkable progress in numerical relativity in the past decade[7] has given detailed results for the GW signals produced. These results, however, do not give a qualitative, phenomenological understanding of the plunge process, an understanding at the same level as that we have for the early inspiral and late QNR. In addition to the satisfaction that such an understanding could provide, there are possible practical advantages. With an intuition about the plunge, computational searches could be guided to particularly interesting scenarios. In this paper we attempt to give a first step, an intersting first step, towards the understanding of the plunge.

### B. Introduction and Summary

We attempt here to give a simple understanding, more precisely a simple view of the generation of plunge radiation and the excitation of QNR. The ultimate goal is a set of guidelines that could allow a complete quasi-analytic

description of merger. It should be noted in this connection that the difficulty posed by the plunge, the end of inspiral and beginning of QNR, has been recognized as a challenge in the effective one body formalism[8].

The result we present is a very simple general picture: the plunge is determined by the conditions of the binary associated with the "light ring," (LR) the location of photon orbits. This picture is supported both by a mathematical reason that the picture should apply, and by a variety of examples. The simple general picture, however, must be viewed as somewhat speculative since it depends on several approximations. By far, the most important of these is the particle perturbation approximation. We have also limited our analysis to nonrotating (Schwarzschild) black holes and, in some aspects of the mathematical analysis, to simplified models. Despite these approximations, we feel that the picture that emerges is very compelling as a first step that can motivate and guide further work.

There has been considerable past work[9–14] reported on the connection between the LR and QN frequencies. Of particular relevance to our current work is the analysis of the multipole content of merger ringdown radiation and the relationship of the start of ringdown to the passage of the particle through the light ring[15]. Our interest here is somewhat different, not only to observe the connection in the radiative signal but to understand its origin, and to understand the transition to the ringdown and the peak of the radiation.

The approach presented in the sections below consists of the following steps. First, in Sec. II we introduce the particle perturbation approximation and the idea of using the Fourier domain Green function (FDGF) to understand, with simple mathematics, the analytic connection between the motion of our point particle and the excitation of plunge radiation and QNR. With this technique, the radiation is reduced to a single, relatively simple, integral over the path of the particle. The use of the FDGF, in fact, is one of the elements of our hope that the plunge can be understood. The basis of that hope is that the QN frequency is a pole in the FDGF. This is true in very broad generality, so the way in which a particle source "excites" a pole should have significant universality. Excitation in a simple model may therefore tell us a great deal about a much more complicated realistic model. With this motivation we introduce, in this section, a model with a very simple FDGF. Even this simple model, however, is complicated enough in its details to be distracting, so most of these details are deferred to an appendix.

Next, in Sec. III we define a class of trajectories that allow for simple analysis combined with sufficient flexibility to test models. In this section, also, we show that the perturbations computed from the FDGF, for the simple model, agree to high accuracy with numerical evolution of initial data. We then, in Sec. IV, use the FDGF to investigate what it is about the trajectory that determines the excitation of QNR. Our investigations in this section are limited to radial motions, since our model is based on a scalar charged particle source of a scalar field. For the scalar case, orbital motion modifies the source with a multiplicative, time dependent angular factor. By contrast, for the gravitational and electromagnetic case, the source term has extra additive terms for angular motion. Our scalar model, therefore, will not give results that are representative of gravitational wave generation, it does however give interesting insights into the excitation of QNR and to the plunge radiation.

Our conclusions from Sec. IV are extended and tested in Sec. V, where we show them to be valid for trajectories in the Schwarzschild background. In this section we include investigations both of radial motion and motion with angular orbital motion and we show in this section that the plunge radiation and QNR are determined by the angular as well as the radial motion of infall.

In Sec. VI, we give a viewpoint on why the LR plays the important role in the generation of QNR. We conclude in Sec. VII and relate the work presented to directions for further investigations. Some details of the complete FDGF are given in Appendix A.

We use units in which $c = G = 1$ and other conventions of the text by Misner, Thorne and Wheeler[16]. The following acronyms will be used throughout the paper: QN=quasinormal; QNR=quasinormal ringing; LR=light ring; FDGF=Fourier domain Green function. We will typically use the capital $T$ to indicate particle time, and the lower case $t$ for other uses, in particular as part of the retarded time of received radiation.

## II. PARTICLE PERTURBATION APPROXIMATION AND FOURIER DOMAIN GREEN FUNCTION

### A. Particle perturbation model

We start by considering a model of a perturbation field $\Phi$ generated by particle motion in a Schwarzschild background. In effect, this particle perturbation model is justified by the fact that it applies in the limit of an extreme ratio of the masses of the binary compact objects[17–20]. But an important question is whether phenomena in the extreme mass limit are qualitatively similar to the phenomena for comparable mass binaries. Many examples show that this does seem to be the case. One such example is the analysis of the antikick phenomenon found with numerical relativity computations for comparable mass[21–23]. With particle perturbation analysis [21, 22, 24] it has been shown that this paradoxical phenomenon has a simple underlying explanation. The current paper uses the history of such

successes as the reason to look for particle perturbation modelling as an appropriate step toward understanding the plunge and the excitation of QNR.

The great advantage of particle perturbation theory is, of course, that the equations describing the fields are linear, and allow the insights of a Fourier transform and, for a spherically symmetric background, of multipole decomposition.

For greatest simplicity we take our model to be based on a scalar perturbation field, $\Phi$, coupled to a scalar-charged particle. We start the analysis by decomposing $\Phi$ into spherical harmonics $r^{-1}\sum_{\ell m}\Psi_{\ell m}Y_{\ell m}$ and by writing the equation for the $\ell m$ multipoles as

$$\frac{\partial^2\Psi_{\ell m}}{\partial r^{*2}} - \frac{\partial^2\Psi_{\ell m}}{\partial t^2} - V_\ell(r^*)\Psi_{\ell m} = S_{\ell m}(r^*,t)\,. \tag{1}$$

Here $r^*$ is the Regge-Wheeler[25] "tortoise coordinate" defined in terms of the standard Schwarzschild areal coordinate $r$, by

$$dr/dr^* = 1 - 2M/r\,. \tag{2}$$

The crucial feature of the $r^*$ coordinate is that it remaps the semi-infinite scope ($2M$ to $\infty$) of the Schwarzschild areal coordinate to $-\infty$ to $\infty$.

The "curvature potential"[26], $V_\ell(r^*)$ depends on the type of field (scalar, electromagnetic, gravitational perturbation)[27]. What is common to all these potentials is that for $r^* \gg M$ the potential has the form of a centrifugal potential,

$$V_\ell(r^*) \longrightarrow \frac{\ell(\ell+1)}{r^{*2}} \quad \text{for } r^* \gg M\,, \tag{3}$$

and that as $r^* \longrightarrow -\infty$ the potentials fall off exponentially in $r^*$, that is, as $(1-2M/r)$. The transition between the flat spacetime centrifugal potential and the dramatically decreasing exponential form occurs around the "light ring," $r = 3M$, the location of circular photon orbits.

For the problem in which we are interested, the source term $S_{\ell m}(r^*,t)$ is a point particle moving in the equatorial ($\theta = \pi/2$) plane with radial position $r^* = F(t)$. The nature of the source term, like the specifics of the potential, depends on details of the model. The source term may contain a delta function, or derivatives of delta functions, or sums of such terms. Our paradigmatic simplest case will be the scalar problem, with a source term that contains only a delta function, not its derivatives. In this case the source will have the form

$$S_{\ell m}(r^*,t) = f(t)\delta\left(r^* - F(t)\right)\,. \tag{4}$$

Here $f(t)$, which in general may depend on $\ell, m$, can be used to represent, e.g., time dependence of scalar charge or, as shall be discussed later, orbital motion. This factor will almost always be taken as $f = 1$, but will be useful in Sec. III for comparing numerical results.

We now change notation in two ways. First, we drop the $\ell, m$ indices which will be clear from the context of the models to follow. Second, we will want to generalize the background rather than be limited to that of the Schwarzschild geometry. Our generalization, in fact, focuses on Eq. (1) as a wave equation in one spatial dimension. To emphasize this, we replace $r^*$ by the coordinate $x$, with the understanding that it ranges from $-\infty$ to $+\infty$. Equation (1), then is replaced by

$$\frac{\partial^2\Psi}{\partial x^2} - \frac{\partial^2\Psi}{\partial t^2} - V(x)\Psi = f(t)\delta\left(x - F(t)\right)\,. \tag{5}$$

### B. The Fourier Domain Green Function

We define the time domain Green function $G(x,a;t-T)$ by the differential equation

$$\frac{\partial^2 G}{\partial x^2} - \frac{\partial^2 G}{\partial t^2} - V(x)G = \delta(x-a)\delta(t-T)\,, \tag{6}$$

and the same boundary conditions that apply to Eq. (1): outgoing radiation (i.e., propagating to larger $x$) at $x \longrightarrow \infty$, and ingoing radiation (i.e., propagating to lower $x$) at $x \longrightarrow -\infty$. Since

$$\delta(x - F[t]) = \int_{-\infty}^{\infty}\int_{-\infty}^{\infty}\delta(a - F[T])\delta(x-a)\delta(t-T)\,da\,dT\,, \tag{7}$$

it follows that the solution to Eq. (5) is

$$\Psi(t,x) = \int_{-\infty}^{\infty}\int_{-\infty}^{\infty} G(x,a;t-T)f(T)\delta(a-F[T])\,da\,dT\,. \tag{8}$$

Next we introduce the Fourier domain Green function (FDGF) $\mathcal{G}$ by

$$G(x,a;t-T) = \frac{1}{2\pi}\int_{-\infty}^{\infty} e^{-i\omega(t-T)}\mathcal{G}(x,a;\omega)d\omega\,, \tag{9}$$

where (from Eq. (6)), $\mathcal{G}$ satisfies

$$\frac{\partial^2\mathcal{G}}{\partial x^2} + \left(\omega^2 - V(x)\right)\mathcal{G} = \delta(x-a). \tag{10}$$

We can put together Eqs. (8) and (9) to get

$$\Psi(t,x) = \frac{1}{2\pi}\int_{-\infty}^{\infty}\int_{-\infty}^{\infty}\int_{-\infty}^{\infty} e^{-i\omega(t-T)}\mathcal{G}(x,a;\omega)f(T)\delta(a-F[T])\,d\omega\,da\,dT\,. \tag{11}$$

### C. The FDGF for a simple model

The FDGF for the Schwarzschild curvature potential has a complicated analytic structure. The infinite set of quasinormal frequencies must appear, and – even worse – there is a branch point at $\omega = 0$ associated with the late-time power-law tails[28]. This complexity is a disadvantage for intuitive insights, and adds significant difficulty to evaluations of Green function solutions. For that reason we illustrate some of the features of our analysis with a model that has a very simple Green function. The truncated dipole potential (TDP)[29] is defined by

$$V = \begin{cases} \ell(\ell+1)/x^2 = 2/x^2 & \text{for } x > x_0 \\ 0 & \text{for } x < x_0 \end{cases}\,. \tag{12}$$

In this simple model, the sharp edge at $x = x_0$ plays the role of the steep dropoff of the Schwarzschild potential for $r$ less than around $3M$. With the substitution of Eq. (12) for the Schwarzschild curvature potential, the solutions to Eq. (10) take an elementary form both for $x < x_0$ and $x > x_0$. Matching conditions then lead to a simple polynomial equation to be solved for the QN frequencies.

There are disadvantages to making the substitution of the TDP for the Schwarzschild potential, both obvious and not. The obvious disadvantage is that the substitution raises the question whether the insights provided will be applicable to the Schwarzschild background. A partial answer to this question is the observation that the phenomenon of complex frequencies occurs in the TDP (and in other truncated multipole potentials). It is reasonable to infer that the excitation of the TDP and the Schwarzschild potential will show *qualitatively* similar dependences on particle motions. The real answer to this question, however, is found in the models of Sec. V; the insights from the TDP model *do* seem to give correct insights into the nature of plunge radiation and QNR in Schwarzschild models.

The not-so-obvious disadvantages of the TDP model are, however, worth a consideration. One of these disadvantages is the "quality factor" of the QN modes, the ratio of the real (oscillatory) part of a QN frequency to the imaginary (damping) part. For the least damped of the Schwarzschild quadrupole modes, the modes of prime importance to GW astrophysics, this ratio is 4.2, while for the single TDP pair of modes it is 1.0. Due to the low quality factor, QNR in TDP radiation does not have the same lightly damped sine wave appearance as for QNR in Schwarzschild models. Worse than this visual inconvenience is the fact that the damping part of the QNR for TDP models is smaller than that for the Schwarzschild models. (More specifically, the TDP damping frequency is $1/(2x_0)$ or $1/6M$ if we associate $x_0$ with $3M$. The Schwarzschild damping frequency $0.088965/M$ is about half of that.) We will argue that QNR is determined by the features of the orbit within a damping time of crossing the LR. The longer damping time for TDP than for Schwarzschild, means that this principle of LR importance is tested more stringently in the TDP models than in Schwarzschild models.

It would be ideal, of course, to have a model for the potential term that has all the features we would like, but for which the FDGF has an elementary form. A sharp cutoff at some $x_0$, as in Eq. (12), guarantees that for $x < x_0$ the Green function has a simple elementary form. The challenge is to find the right form of $V(x)$ for $x > x_0$. One such possibility is the Pöschl-Teller potential[10], $\mathrm{sech}^2 x$, but this potential does not approach the flat spacetime centrifugal potential at large $x$ and hence is a questionable subsitution. An obvious question is why we do not use a higher order

truncated multipole potential, i.e., $\ell(\ell+1)/x^2$, with an integer $\ell$ larger than unity. For all such potentials the Green function has only elementary functions. As $\ell$ increases, however, the Green function – though elementary– becomes more and more complicated. Furthermore, the quality factor of the least damped QN mode increases slowly with increasing $\ell$. We would have to go to $\ell$ of order 10 to get a ratio of damping to oscillation that is qualitatively similar to QNR in the Schwarzchild geometry[30].

The complete FDGF for TDP, and its derivation, are given in Appendix A. The explicit expressions for the FDGF depend on the relative location of $x$, $x_0$, and particle position $a$, but all expressions are simple. As an example, for $a < x_0 < x$ the expression is

$$\mathcal{G} = -\frac{i}{2}\frac{e^{-i\omega(a-x)}\omega}{(\omega-\omega_1)(\omega-\omega_2)}\left(1+\frac{i}{\omega x}\right), \tag{13}$$

where $\omega_{1,2}$ are the TDP QN frequencies

$$\omega_1, \omega_2 = -\frac{i}{2x_0} \pm \frac{1}{2x_0}, \tag{14}$$

which show up, as expected, as poles in the FDGF.

For a known trajectory $x = F(T)$, we can find the solution to Eq. (5), for $x > x_0$, at all times, by using $\mathcal{G}$ of Eq. (13) for $a < x_0$, and the Green function (in Eq. (A2)) for $a > x_0$. To do this we introduce notation for times of importance $T_{\rm cross}$ and $T_6$, important times along the trajectory. (The notation $T_6$ arises from the step-by-step development of the TDP FDGF in Appendix A.) These times, and the integration variables $\theta$ and $\xi$, are defined by

$$F(T_{\rm cross}) = x_0 \qquad T_6 - F(T_6) = t - x \tag{15}$$

$$\theta = (t - T + F(T) - x)/(2x_0) \qquad \xi = (t - T - x - F(T) + 2x_0)/(2x_0)\,. \tag{16}$$

We take $f(t) = 1$; the solution is then

$$\Psi = \frac{x_0}{2}\int_{T_{\rm cross}}^{T_6} e^{-\theta}\left[\frac{1}{x_0}(\sin\theta - \cos\theta) - \frac{2}{x}\sin\theta\right] dT$$

$$-\frac{1}{2}\int_{-\infty}^{T_{\rm cross}} e^{-\xi}\left[-(\cos\xi + \sin\xi) + 2x_0\left(\frac{1}{F(T)} + \frac{1}{x}\right)\cos\xi - \frac{2x_0^2}{xF(T)}(\cos\xi - \sin\xi)\right] dT\,. \tag{17}$$

The second integral extends to $T_{\rm cross}$, the time at which the particle, moving inward, passes the potential "edge" at $x = x_0$. This integral represents the contributions to the field from the pre-crossing motion; the first integral gives the contribution for the motion subsequent to the edge passage.

## III. TEST TRAJECTORY

To investigate the generation of radiation, we must choose particle trajectories for the Schwarzschild background, for our TDP, or for the other models that we will introduce below. There are several features we would like in a family of trajectories. First, we would like all trajectories in the family to conform to the analog of the physical constraints on trajectories in the Schwarzschild background. The most fundamental of these constraints is that $dr^*/dt \to -1$ as the particle approaches the horizon. For our trajectory family to be used with Eq. (5) we therefore require $dx/dt \to -1$ as $x \to -\infty$.

We also require that the trajectories belong to a family with at least two parameters. In this way, we can compare the radiation for a range of trajectories with one feature of the trajectories fixed. It is in this way that we will argue that the plunge radiation and QNR are not sensitive to the nature of the trajectory away from the edge.

A third criterion for a family of trajectories is one of convenience. As a check on details, it is useful to compare the computation of $\Psi$ done with the FDGF integrals, like those in Eq. (17), to the solution found by evolving initial data in the standard manner used in numerical relativity. For such evolution, we need initial data, and the most convenient initial data is static initial data, i.e., the fields that would exist at time zero if the particle had been sitting in a fixed position forever, and only started to move at time zero. Note that the motion before time zero is needed not only for evolution codes, but is also needed for the Green function solution, since the integrals, e.g., the second integral in Eq. (17), require a specification of the particle position back to the infinite past. For static initial data,

both $\partial\Psi/\partial t$ and $\partial^2\Psi/\partial t^2$ must vanish at time zero. This in turn means that for our trajectories both the velocity and acceleration must be zero at time zero.

A desideratum, though not a requirement, is that the family of trajectories leads only to simple closed form analysis. The following two-parameter family for the radial motion, our "cubic trajectory" family, satisfies this as well as the three criteria above:

$$F(T) = \begin{cases} a_0 + \tau - \left(T^3 + \tau^3\right)^{1/3} & T > 0 \\ a_0 & T < 0\,. \end{cases} \tag{18}$$

The two parameters are $a_0$, the initial $x$ position of the particle, and $\tau$, the timescale on which the particle accelerates. For $T > 0$, both the velocity $v$ and acceleration $a$ (not to be confused with "$a$" used in the previous section as a proxy for $F(t)$) are

$$v = -T^2\left(T^3 + \tau^3\right)^{-2/3} \qquad a = -2T\tau^3\left(T^3 + \tau^3\right)^{-5/3}\,, \tag{19}$$

and both go to zero as $T \to 0$.

The cubic trajectory can be inverted in closed form to give $T$ in terms of $F$. What is actually required for computations are the solution for $F(T) \pm T$. In the $F(T) - T$ case we must solve

$$T + \left(\tau^3 + T^3\right)^{1/3} = \rho\,, \tag{20}$$

where $\rho$ is a known function of $t, x, a_0, \tau$. The cubic equation that results has the closed form solution

$$s \equiv \sqrt{\frac{\tau^6}{16} + \frac{\rho^6}{64}} \qquad A \equiv \left(-\frac{\tau^3}{4} + s\right)^{1/3} \qquad B \equiv -\left(\frac{\tau^3}{4} + s\right)^{1/3} \qquad T = A + B + \frac{\rho}{2}\,. \tag{21}$$

In the $F(T) + T$ case, the problem requires solution of

$$T - \left(\tau^3 + T^3\right)^{1/3} = -\sigma\,, \tag{22}$$

where $\sigma$ is a known function of the trajectory parameters. By transposing one of the terms from the left to the right, and raising both sides to the third power, the $T^3$ terms cancel, leaving a quadratic equation which has the solution

$$T = \frac{1}{2}\left(-\sigma + \sqrt{\frac{4\tau^3}{3\sigma} - \frac{\sigma^3}{3}}\right)\,. \tag{23}$$

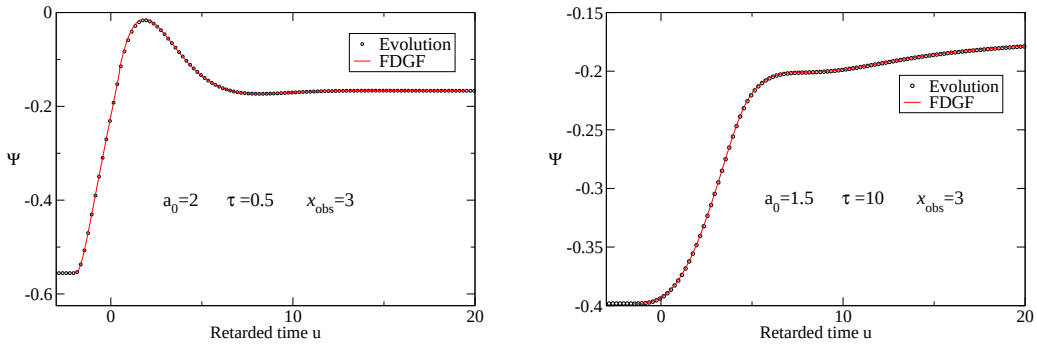


FIG. 1: Comparison of computations with the Fourier domain Green function and with numerical evolution for radial infall. The scalar TDP test field $\Psi$ is given as a function of retarded time $u$. All values are given in units of the edge location $x_0$. The particle generating the field moves according to the cubic trajectory of Eq. (18) with the parameters shown in each plot. The particle has been stationary at $a_0$ prior to $T = 0$.

Figure 1 shows the comparison between numerical evolution of the partial differential equation in Eq. (5), and the evaluation of the FDGF, for radial infall, with $f(t) = 1$, starting from stationary initial data at $t = 0$ and following the

cubic trajectory of Eq. (18). In this figure, and in those that follow for the TDP, the scaling is set by $x_0$, in a manner parallel to the scaling set in the Schwarzschild geometry, in geometrized ($c = G = 1$) units, by the mass parameter $M$. Thus, for example, a retarded time $u = 50$ is understood to mean $u = 50x_0$ and an acceleration $a = 0.01$ is understood to mean $a = 0.01/x_0$. Note that $\Psi$ itself is also proportional to $x_0$.

The FDGF integrals were carried out using a straightforward Simpson's rule scheme. The evolution scheme is the well-known second-order, Lax-Wendroff finite-difference scheme for second-order 1+1 linear hyperbolic equations; the delta function is represented by a narrow Gaussian, and the boundary conditions are taken to be no incoming waves from $x = \pm\infty$. The TDP field $\Psi$, computed, or "observed," (i.e., numerically extracted) at $x = 3$ is shown as a function of retarded time $u = t - x$. (The choice of a relatively small value of the extraction radius means that the results test all the terms in the TDGF, not only the terms in the radiation zone.) Although the results shown here are limited to the spacetime region $x > x_0$, and $x > F(T)$, computations in other regions showed the same excellent agreement.

For a scalar charged particle falling with angular motion $\phi = \tilde{\phi}(t)$, the source term on the right of Eq. (6) has an additional factor of $\delta(\phi - \tilde{\phi}(T))$. (Though angular motion in our scalar model is not representative of the change in the source for gravitational waves, it remains a useful check on the agreement of the FDGF and evolution.) To compute $\Psi(t, x, \phi)$ for the $\ell = m = 1$ multipole moment we must insert $f(t) = \exp(\pm i(\phi - \tilde{\phi}(T))$ into Eq. (11). To check that the FDGF integrals and numerical evolution agree for orbital motion, we take $\phi = 0$, and we extract the real part of $\Psi$, i.e., we insert $\cos\tilde{\phi}(T)$ in the integral. In order to have the angular, as well as radial motion start with zero acceleration, we take the angular motion to be

$$\tilde{\phi}(T) = \phi_0 \left[ \frac{\left(T^3 + \tau^3\right)^{1/3} - \tau}{\left(T^3_{\rm cross} + \tau^3\right)^{1/3}} \right] . \tag{24}$$

With this choice, orbital motion starts at $\phi = 0$ with zero angular velocity and angular acceleration.

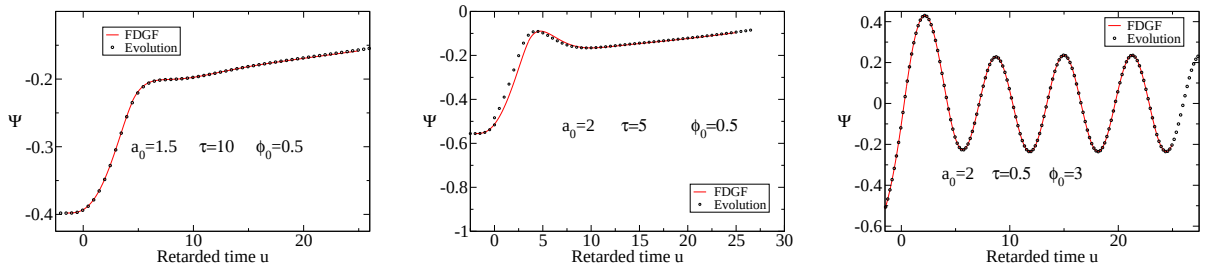


FIG. 2: Comparison of computations with the Fourier domain Green function and with numerical evolution for orbiting infall. The radial motions are those described by Eq. (18), with the trajectory parameters indicated in each plot; values are given in units of the edge location $x_0$. The source has been modified with the angular factor $\cos\tilde{\phi}(T)$, as described in Eq. (24). The examples give comparisons of three orbits that are qualitatively very different.

Figure 2 shows the comparison between numerical evolution and evaluation of the FDGF for orbiting infall starting from this stationary initial data at $t = 0$. The $x$ position of the particle follows the cubic trajectory of Eq. (18) and the azimuthal angle is given by Eq. (24). Note that this orbital motion is not physical. The angular motion is not compatible with the conservation of angular momentum in the Schwarzschild background which our TDP is meant to model. This, however, is not relevant to the current purpose of testing the consistency of evolution and FDGF computations.

## IV. QNR FROM RADIAL INFALL

### A. The mathematics of QNR excitation

To obtain insights into the plunge radiation and the excitation of QNR in the TDP, we look at a typical scenario in which a particle starts outside the edge of the TDP (in terms of Eq. (18), $a_0 > x_0$), crosses the edge (at a trajectory time $T_{\rm cross}$), and continues to fall in. The FDGF integrals in Eq. (17) describe this scenario. We can make this simple

integral even simpler by considering only the radiation zone, i.e., by ignoring the part of $\Psi$ that falls as $1/x$. This leaves us with

$$\Psi = \frac{1}{2}\int_{T_{\rm cross}}^{T_6} e^{-\theta}\,(\sin\theta - \cos\theta)\;dT - \frac{1}{2}\int_{-\infty}^{T_{\rm cross}} e^{-\xi}\left[\left(\frac{2x_0}{F(T)} - 1\right)\cos\xi - \sin\xi\right] dT\,. \tag{25}$$

We will call the integral involving $\theta$'s the "late" (after edge crossing) integral, and the one involving $\xi$'s the "early" (prior to edge crossing) integral and we start our analysis with the late integral. The expression for $\theta$ is illustrated in Fig. 19 of Appendix A, in which a complete description is given of the FDGF. That figure, and the discussion connected to it, show that the late integral expresses the influence of the particle, consistent with causality, on the spacetime point at retarded time $u$. What is of special importance is the "damping," i.e., the falloff of influence dictated by the factor $e^{-\theta}$.

To understand the role of this damping factor, we note that for any value of $u$, the damping factor is unity when $\theta = 0$, that is, the contribution is maximum from the point on the trajectory labeled $T_6$ in Appendix A. The time $T_6$, by causality, is the latest time on the trajectory that can influence the field at retarded time $u$. Contributions from earlier points on the trajectory, at time $T_6 - \Delta T$, are damped by $e^{-\Delta\theta}$ with

$$\Delta\theta = \left(\Delta T + [F(T_6 - \Delta T) - F(T_6)]\right)/2x_0 \approx (1 + v_6)\,\Delta T/2x_0\,, \tag{26}$$

where $v_6 = |dF/dT|$, the speed of the trajectory at $T_6$, is a positive quantity.

At the most basic level, this result shows that for the contribution to the late integral at any value of $u$, the trajectory is relevant only for a trajectory time less than or roughly comparable to the damping time $2x_0$. It also shows that the only property of the trajectory that matters is the velocity at $T_6$, unless the velocity changes substantially over a time comparable to one damping time, i.e., only if $|d^2F/dt^2|$ is comparable to $2x_0|dF/dt|$.

A useful insight comes from changing the integration variable in the first integral of Eq. (25) to $\theta$, so that the integral becomes

$$\Psi_{\rm late} = x_0\int_0^{\theta_{\rm cross}} e^{-\theta}\,\frac{(\sin\theta - \cos\theta)}{1 + v(\theta)}\,d\theta\,, \tag{27}$$

where $v(\theta)$ is $|dF/dT|$ expressed as a function of $\theta$ rather than $T$. If the velocity changes very little over the range of $T$ during which most of the contribution to the integral occurs, then we can approximate $v(\theta) = v_{\rm cross}$ in Eq. (27) to get

$$\Psi_{\rm late} = \frac{x_0}{1 + v_{\rm cross}}\int_0^{\theta_{\rm cross}} e^{-\theta}\,(\sin\theta - \cos\theta)\;d\theta = -x_0\frac{e^{-\theta_{\rm cross}}\sin\theta_{\rm cross}}{1 + v_{\rm cross}}\,. \tag{28}$$

This means that the peak of $\Psi$ occurs at $\theta_{\rm cross} = \pi/4$, or at

$$u_{\rm peak} - u_{\rm cross} = u_{\rm peak} - T_{\rm cross} + x_0 = \pi/4 \tag{29}$$

and that the value of $\Psi$ at the peak is

$$\Psi_{\rm late,peak} = -\frac{x_0\sqrt{2}\,e^{-\pi/4}}{\pi\,(1 + v_{\rm cross})}\,. \tag{30}$$

We noted that only the velocity at crossing can matter. These results show that, in fact, for the late integral the location of the peak of the radiation is independent of that velocity, and the strength of the radiation is very insensitive to the velocity. A better statement, then, is that the radiation described by the late integral is approximately independent of any feature of the trajectory.

Though it is a reasonable approximation to take the velocity to be constant in the late integral, it is not useful to take $F(T)$ to be a constant (in particular, to be $x_0$) in the second integral in Eq. (25). Graphical insights, however, do follow from Figure 3. The figure shows the two sources of the radiation at the "observation" event at retarded time $u$. The 45°, "speed of light," line from $T_6$ to the observation event illustrates that $T_6$ is the latest time on the world line that can influence that event. This, then is the graphical explanation of why the upper limit in the early integral in Eq. (25) is at $T_6$. The lower limit in this early integral is at $T_{\rm cross}$ because all of the integral in Eq. (25) arises from the TDGF for $F(T) < x_0$; for $T < T_{\rm cross}$ the particle has not yet crossed that edge.

It is intuitively obvious that the edge at $x_0$ must be involved in QNR. This raises a natural question about the early integral in Eq. (25). Since this integral is over only $T \leq T_{\rm cross}$, its radiation features would seem not to be influenced by the existence of the edge. How can it, therefore, contribute to QNR? The question is answered graphically in Fig. 3; the early integral involves radiation that has interacted with the edge via the dashed path in Fig. 3. We can see this in the form of $\xi$ in Eq. (16). Notice that the total distance traversed along the dashed line in Fig. 3 is the sum of the inward distance $F(T) - x_0$ and the outward distance $x - x_0$. The total time is $t - T$. It follows that $\xi$ is simply the total time minus the distance traversed, so that causality requires that $\xi$ be greater than 0. But $\xi = 0$ is equivalent to the $T = T_{\rm cross}$ upper limit of the the early integral.

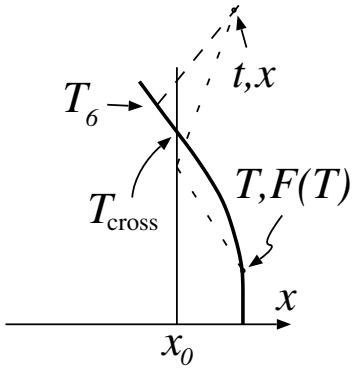


FIG. 3: A spacetime diagram showing the influence of the particle on the "observation" point at retarded time $u = t - x$. The dashed 45° line indicates the direct, speed-of-light causality connecting the particle position at $T_6$ with the observation point, and showing that $T_6$ is the latest point on the particle world line that can influence observation at retarded time $u$. The "slower than light speed" dashed lines indicate influence from earlier times via reflection from the edge at $x_0$.

It is important to understand that the "slower than light" propagation involved in the early integral is not a manifestation of strong spacetime effects. Rather, it is associated with the fact that we are working with a multipole decomposition. The influence of a particle's multipole moments on the radiation signal at an event, comes from all angles. The radial characteristics, then, are only an indication of the limiting speed with which multipolar information propagates.

### B. Models for cubic trajectories and TDP

As the first test of the QNR excitation principle explained above, we look at a scalar charge following a radial trajectory in the TDP background. We use the radial trajectory function denoted by $F(T)$ and defined in Eq. (18). From that equation and

$$F(T_{\rm cross}) = x_0$$

we have that

$$T_{\rm cross} = \left[(a_0 + \tau - x_0)^3 - \tau^3\right]^{1/3} . \tag{31}$$

Once $T_{\rm cross}$ is known, the velocity and acceleration at crossing can be found from

$$v(T_{\rm cross}) = \frac{d}{dT}F(T)\bigg|_{T=T_{\rm cross}} = -\frac{{T_{\rm cross}}^2}{(\tau^3 + {T_{\rm cross}}^3)^{2/3}}, \tag{32}$$

$$a(T_{\rm cross}) = \frac{d^2}{dT^2}F(T)\bigg|_{T=T_{\rm cross}} = -\frac{2T_{\rm cross}\tau^3}{(\tau^3 + {T_{\rm cross}}^3)^{5/3}}. \tag{33}$$

In all our models the velocity and acceleration are nonnegative. For simplicity, we will use the absolute values of these quantities in our discussions below, i.e.,

$$v_{\rm cross} \equiv |v(T_{\rm cross})|, \tag{34}$$

$$a_{\rm cross} \equiv |a(T_{\rm cross})|. \tag{35}$$

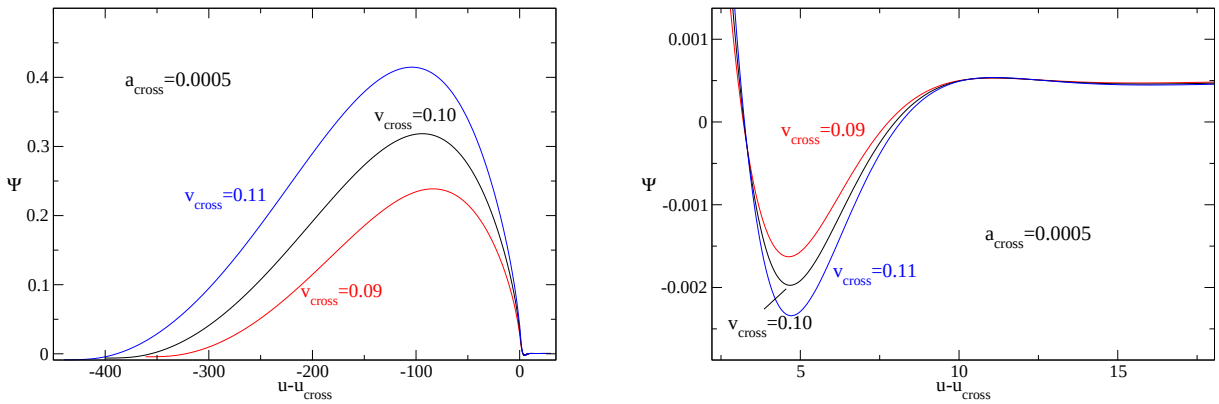


FIG. 4: The radiation due to a particle in radial infall in the TDP background. The horizontal axis is the retarded time after the edge crossing value $u_{\rm cross} \equiv T_{\rm cross} - x_0$. The retarded time and $\Psi$ are given in units of $x_0$; the acceleration is given in units of $1/x_0$. The panel on the right focuses on the region of the curves with the peak QNR.

The radiation profiles for several radial infall trajectories, for three different values of $v_{\rm cross}$, are shown in the two panels of Fig. 4. As in Figs. 1 and 2, the scale of length is set by $x_0$. All three trajectories have an acceleration $a_{\rm cross} = 0.0005/x_0$. As a rough estimate, this acceleration multiplied by the damping time ($2\pi$ divided by the imaginary part of the TDP QN frequency $1/2x_0$) gives approximately $\Delta v = 0.01$, on the order of a tenth of the crossing speed of the trajectories. It should, therefore, be a reasonable approximation to consider the infall speeds to be constant during the plunge and excitation of QNR. (Values of acceleration much smaller than $0.0005/x_0$ turn out not to be as useful in demonstrating features of the results.)

In the left panel the initial positive peaks are *not* QNR. Those large peaks, prior to QNR, are analogous to the GWs from the pre-QNR plunge, and we shall call these the "plunge peaks." The QNR, a much less prominent feature of the profile, starts around $u = u_{\rm cross}$, and can be seen as a small negative dip. The stark contrast of this subtle feature with the very visible QNR in the Schwarzschild problem is ultimately due to the fact the QNR damping frequency is equal to the QN oscillation frequency in the case of the TDP. In the Schwarzschild case, the QNR damping frequency is about a quarter of the QNR oscillation frequency.

What is particularly important to notice is that the QNR in the right panel does not agree with the predictions in Eqs. (29) and (30). The QNR peak does not occur reasonably close to $u - u_{\rm cross} = \pi/4$, nor is the peak value of $\Psi/x_0$ approximately -0.19 as predicted by (30). The dependence on $v_{\rm cross}$, in fact is markedly different from that in (30); while the equation predicts a peak that decreases very slightly with increasing $v_{\rm cross}$, the results show a significant *increase* in the peak with increasing $v_{\rm cross}$. This cannot be attributed to the fact that the infall speed is not exactly constant; in fact, the numerical evaluation of only the "late" integral for the trajectories in Fig. 4 agrees to high accuracy with the predictions of Eqs. (29) and (30). Rather, we learn from Fig. 4 that the QNR is dominated by the "early" integral, the second integral in Eq. (25). This is somewhat surprising, and is the first indication of how one might think about the origin of what is the dominant part of GW radiation in a binary merger.

The question remains whether the plunge and QNR are determined only by the infall speed. In flat spacetime, after all, the generation of radiation is associated with acceleration. There is no hint of this in the integrals in Eq. (25), and it is confirmed with the numerical results in Fig. 5 for different accelerations. With an acceleration of $0.001/x_0$, for a damping time $4\pi x_0$, there should be an increase in infall speed on the order of $\Delta v \sim 0.01$. The increase in acceleration, with $v_{\rm cross}$ fixed implies a larger speed after crossing and a smaller speed before. In Fig. 4, we saw that a decrease in both the plunge peak and the QNR excitation is associated with a smaller speed (in the case of a very nearly constant speed). The decrease in plunge peak and QNR excitation therefore reinforces the conclusion that it is the particle motion prior to edge crossing that plays the dominant role in generating this radiation. The argument is strengthened by noting that to very rough order of magnitude the effect of the change of acceleration is of the right size.

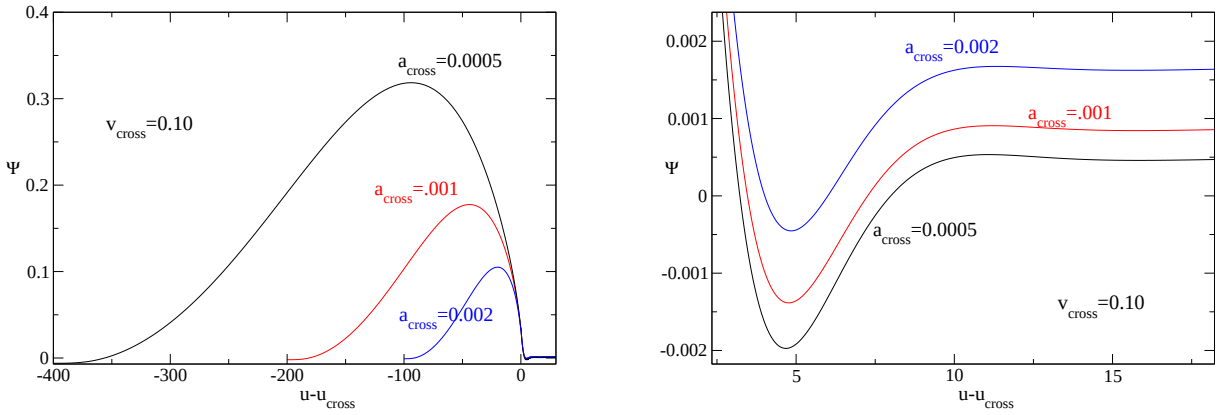


FIG. 5: The radiation due to a particle in radial infall in the TDP background. The horizontal axis is the retarded time $u = t - x$. (See the text for an explanation of units.) The retarded time when the first signal from the potential edge arrives is indicated by $T_{\rm cross}$. Also shown in the figure is the quasinormal oscillation, the only half cycle discernible at this scale for the velocity and acceleration at crossing.

## V. PLUNGE AND QNR FOR TRAJECTORIES IN THE SCHWARZSCHILD GEOMETRY

We emphasize that the simple TDP models above are exploited to give insights into the way in which the trajectories influence the plunge radiation and QNR. Whether they give the right insights for the black hole problem is a distinct question, a question we take up in this section. We use second-order Lax-Wendroff, finite-difference evolution codes[32] for the Teukolsky function $\psi_4$, with our flexible cubic trajectories, to investigate whether, as in the models of the previous section, the plunge and QNR excitation depend only on the conditions at the "edge" of the potential. For this purpose, we take the edge of the potential to be at $r = 3M$. (The physical justification for the importance of the LR is discussed in Sec. VI.)

Some comments need to be made about the way in which we judge and compare the size of QNR. Two issues arise here: First is the fact that unlike the ringing of normal modes, QNR has an amplitude that depends on time. We must therefore find a way in which the magnitude we ascribe to QNR is independent of the time at which we measure the amplitude. The second issue is that we are only looking at the real part of $\psi_4$; might the imaginary part contain different information?

A satisfactory solution to both of these issues is to "remove" the damping from the radiation. To compare results for models with different trajectories, we can multiply all curves to be compared by $\exp(0.088965\, t/M)$, using the imaginary part, $0.0889/M$, of the dominant (least damped) quadrupole Schwarzschild QN mode, the mode of greatest astrophysical relevance. This leads to QNR having a time-independent amplitude, thereby facilitating a comparison of the excitation of QNR with different phases. It also shows us that the real and imaginary parts of $\psi_4$ have the same amplitude once the damping is removed, so no information is lost by plotting only the real part of $\psi_4$.

While this technique may be a very useful tool for working with QNR in other contexts, here we will use it explicitly only near the end of this section, to aid in comparing QNR with different phases. For the most part, the main value of this technique in the current paper is to assure us that we are not missing anything. The lessons contained in the curves presented below demonstrate the insights of interest, without a need for a more careful extraction of QNR amplitude.

### A. Models for radial infall

We start by considering radial infall, with $r^* = F(t)$, in which $F$ is given by Eq. (18), and in which $r^*$ is the solution of Eq. (2) taken to be $r + 2M \ln(r/2M - 1)$. The models that are the basis for Fig. 6 are chosen all to have the same inward speed, $v_{\rm LR} = 0.3$ at the LR. (In this figure, and all those for the Schwarzschild spacetime, numerical values are given in terms of the geometrized ($c = G = 1$) Schwarzschild mass $M$.) Different trajectories, with this same LR speed, are created by varying the $\tau$ parameter of Eq. (18). (The value of $a_0$ is then adjusted so that $v_{\rm LR} = 0.3$.) For a wide range of $\tau$ values, Fig. 6 shows that there is almost no difference in the amplitude or phase of the QNR, and that

there are moderate differences in the peak of the radiation at the plunge transition. Though the QNR has negligible

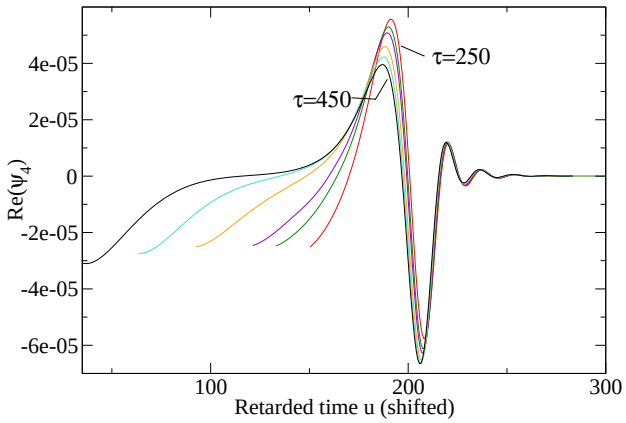


FIG. 6: The plunge radiation and QNR in the real part of the Teukolsky function $\psi_4$ for radial cubic trajectories, all with $v_{\rm LR} = 0.3$ at the $r = 3M$ LR, but with different values of the $\tau$ parameter for the cubic trajectories of Eq. (18). The values of time are shifted so that all trajectories arrive at the $r = 3M$ LR at the same time. The values of $\tau$ range from 250 to 450. The peak around $u = 190$ has a monotonically decreasing height with increasing $\tau$. Note that this peak is not pure QNR, but rather a transition to QNR. The curves shortly after the peak show the QNR, and demonstrate remarkable agreement in the amplitude and phase of the QNR for the different trajectories.

variation, the trajectories themselves vary considerably. We illustrate this in Fig. 7 which compares $r^*(T)$ for the extreme cases $\tau = 250$ and $\tau = 450$. We show in Fig. 8 the opposite of what is shown in Fig. 6. Here all trajectories

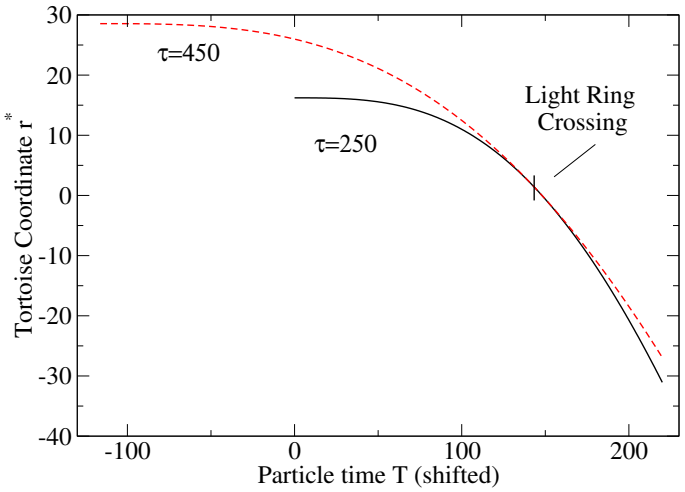


FIG. 7: Trajectories are shown for the $\tau = 250$ and $\tau = 450$ cases of Fig. 6. The tortoise coordinate location $r^*$ of the particle is shown as a funtion of particle time $T$, according to the cubic trajectory of Eq. (18). For the $\tau = 450$ trajectory, the time has been shifted so that the two trajectories arrive at the $r = 3M$ LR at the same value of $T$. Note that the trajectories differ significantly both before and after the LR crossing.

have $\tau = 250$, while the LR speed $v_{\rm LR}$ varies from 0.28 to 0.32. From the form of the trajectories, we find that the acceleration at LR crossing has a magnitude of approximately $2T_{\rm cross}/\tau^2$, which gives a value of approximately $0.0046/M$ for $\tau = 250$ and $0.0026/M$ for $\tau = 450$.

What insights can be gained from a comparison of the TDP results and the Schwarzschild results for radial infall? In the Schwarzschild case the LR plays the role of the edge. This "edge" is not sharply defined as in the TDP

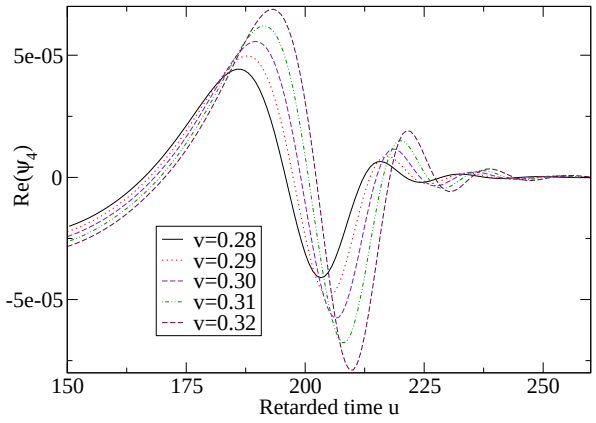


FIG. 8: The radiation from the plunge and the QNR in the real part of the Teukolsky function $\psi_4$ for radial cubic trajectories, all with $\tau = 250$, but with different values of $v = |dF/dT|$ at the LR ($r = 3M$). The retarded time for the curves has been shifted, so that all trajectories pass the LR at the same time.

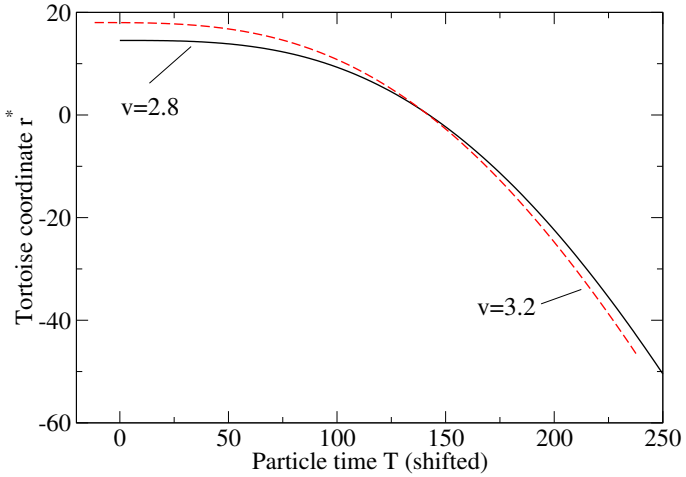


FIG. 9: Trajectories for $v_{\rm LR} = 0.28, 0.32$ and $\tau = 280$, the two extreme examples in Fig. 8. The trajectories are exactly the same shape since in Eq. (18) they differ only in $a_0$, and hence in the speed when they cross the LR. In the figure, the $v_{\rm LR} = 0.32$ curve is shifted so that its LR crossing time agrees with that for $v_{\rm LR} = 0.28$.

case. Another, perhaps more important difference from the TDP case is the longer damping time. These differences result in an important difference in the nature of the generation of the plunge radiation and QNR. In the TDP case this generation was dominated by the early, pre-edge, motion. In the Schwarzschild case the generation seems to be dominated by the late motion. Notice in particular that in Fig. 6 the retarded time (after crossing the LR) and amplitude of the QNR are almost independent of the speed at the LR. This was a specific prediction for the TDP provided that the QNR is dominated by the particle's motion after crossing the potential edge. This prediction translates very well to the Schwarzschild case since the late (post-LR) contribution should be described by a FDGF like that in Eq. (13), with the TDP poles replaced by the Schwarzshild quadrupole GW poles. (To be sure, there will be additional functions of $\omega$, but these will play the role of constants in the evaluation of the residues at the QN poles.) This implies that the late QNR excitation will be governed by an integral analogous to the late integral in Eq. (25). The results in Fig. 6 therefore tell us that the late radiation dominates the excitation of QNR.

Another, somewhat surprising, conclusion can be drawn from these results for Schwarzschild radial infall. Figure 8 shows the plunge radiation increasing with increasing speed at the LR. This is analagous to the TDP plunge radiation

increasing with increasing speed at the potential edge. Insights can then be taken from Fig. 6. The plunge radiation is larger for larger acceleration (smaller $\tau$) at a given crossing speed. This is the reverse of what is seen in the TDP results, for which greater acceleration means smaller plunge radiation. Just as the TDP results indicated that the plunge radiation is dominated by the early (pre-crossing) motion, the Schwarzschild results indicate that the plunge radiation is dominated by the late, post-crossing radiation.

### B. Models for orbital trajectories

As in the radial case, it should only be the motion near the LR that is relevant to the generation of plunge radiation and the excitation of QNR. This suggests that when there is angular velocity $\omega \equiv d\phi/dt$, it is the angular velocity $\omega_{\rm LR}$ at the LR that is important, as well as the radial velocity $v_{\rm LR}$.

If we are to investigate our hypothesis that plunge radiation and QNR excitation is determined only by the conditions, in this case the angular velocity, at the LR, then we need at least a two-parameter family of trajectories for $\omega(r)$ or $\omega(t)$, and for clarity of analysis we would like to vary the orbital motion for a fixed choice of radial motion. As we have explained for radial motion, the models need not be limited to families of trajectories that are physically correct motions. In the case of angular motion, however, we *do* need to consider several physical limitations on the nature of $\omega$. First, the orbital angular velocity $d\phi/dt = \omega$ is redshifted. That is, $\omega$ dies off as $(1 - 2M/r)$ as the particle approaches the horizon. It turns out that we must choose orbital motions that respect this condition. If we do not, then the plunge radiation and QNR, for interesting values of $\omega_{\rm LR}$, are hidden by the much larger radiation coming directly from the particle motion.

A second feature of physically correct angular motion is that $d\omega/dt = 0$ at the LR. If we were to retain this feature it would hamper the demonstration that it is only the value of $\omega$ at and near the LR that is important. Though this feature hampers our demonstration, it supports our hypothesis. Since $\omega$ near the LR is not very different from at the LR, our hypothesis would be wrong only if conditions on $\omega$ far from the LR would be important.

A third, and obvious, physical feature of orbits is that they must not exceed light velocity. In our notation, with $v_{\rm LR} \equiv -dr^*/dt$ at the LR, this condition is $27\omega_{\rm LR}^2 M^2 < 1 - v_{\rm LR}^2$. Though this is a physical constraint on $\omega_{\rm LR}$ it need not be a constraint on our exploration of the nature of the plunge radiation and QNR.

Our choice is to take the angular motion to be

$$\omega = \omega_{\rm LR}\, \frac{27M^2}{(1+\sigma)r^2} \left(1 - \frac{2M}{r}\right) \left(1 + \frac{3\sigma M}{r}\right) , \tag{36}$$

in which $\omega_{\rm LR}$ appears explicitly as one of the parameters. For all values of the two parameters, $\omega$ in this model has the physically correct redshift. The parameter $\sigma$ governs $d\omega/dt$ at the LR. For $\sigma > 0$, in our models, the angular frequency $\omega$ increases as the particle moves inward past the LR.

We start the investigation of the effects of orbital motion by asking what is the interesting range of values of $\omega_{\rm LR}$. Results of evolution codes are shown in Figs. 10 and 11. For the models shown the radial speed as the LR is crossed is $v_{\rm LR} = 0.3$, so that the speed-of-light limit on $\omega_{\rm LR}$ is $0.1836/M$. And for all models shown in Figs. 10 and 11, the $\sigma$ parameter in Eq. (36) is taken to be $\sigma = 1$. The results in Fig. 10 are for very small values of $\omega_{\rm LR}$, values that do not exceed the light speed limit. For all these models, the post-plunge radiation (waveforms after $t/M$ is 548.9) is QNR. For the smallest value $\omega_{\rm LR} = 0.005/M$ the result is indistinguishable from pure radial infall. This is to be expected since this value is much smaller than the imaginary (damping) part of the QNR frequency, $0.088965/M$. From the FDGF point of view this means that the motion of the source due to angular velocity is insignificant until the damping factor has reduced the QNR excitation integral to a negligible size.

As $\omega_{\rm LR}$ increases to a value comparable to the imaginary part (0.0889/M) of the QNR frequency, the orbital motion starts to have an effect, increasing both the plunge radiation and the excitation of QNR. For $\omega_{\rm LR} = 0.01/M$ both can be seen to be distinguishable from that for $\omega_{\rm LR} = 0.005/M$. With a further increase of the value of $\omega_{\rm LR}$, to a value still within the speed-of-light limitation, the effect of orbital motion becomes dramatic.

Figure 11 shows the post-plunge radiation for values of $\omega_{\rm LR}$ approaching and exceeding the light speed limit. In the models shown, the post-plunge radiation for both $\omega_{\rm LR} = 0.05/M$ and $0.10/M$ have a period of the same order as the period $16.81\,M$ of the least damped Schwarzschild QN mode. (This period is shown as a horizontal bar.) For $\omega_{\rm LR} = 0.5/M$, the very large oscillations are at a clearly different and noncostant frequency. As models progress from $\omega_{\rm LR} = 0.1/M$ to higher frequency, the late time results are no longer pure QNR, but are QNR increasingly mixed with some higher frequency radiation. Below, in subsection V C, we demonstrate that for $\omega_{\rm LR}$ well above the QNR frequency what we are seeing is radiation coming directly from the motion of the particle.

Orbital frequencies well above that of QNR are unphysical, so we presently limit our considerations to $\omega_{\rm LR}$ below 0.10 or so, and we return to the central question of this paper in the context of this subsection: Are plunge radiation and the excitation of QNR determined primarily by $\omega_{\rm LR}$, and not by the angular motion at other radii? To investigate this

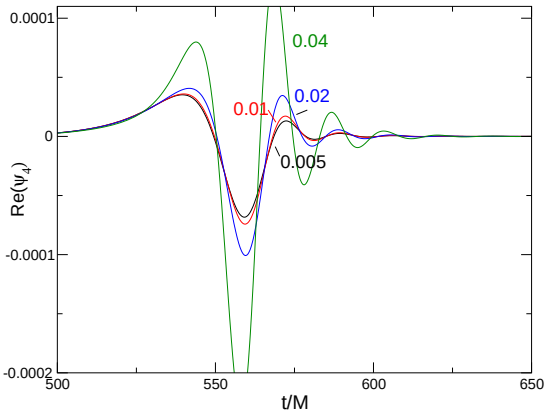


FIG. 10: Plunge radiation and QNR excitation from models with angular frequency $M\omega_{\rm LR}$ =0.005, 0.01, 0.02, 0.04. All models have radial motion for $a_0 = 38.6114\,M$ and $\tau = 600\,M$, and hence in all cases the particles pass the LR at time $T_\times = 348.90\,M$, with a speed $v_{\rm LR} = 0.3$. For all orbital motions, $\sigma = 1$. Note that each waveform shown is extracted at $r^* = 200\,M$, implying that the waveform at $T \approx 550$ originates at the LR crossing.

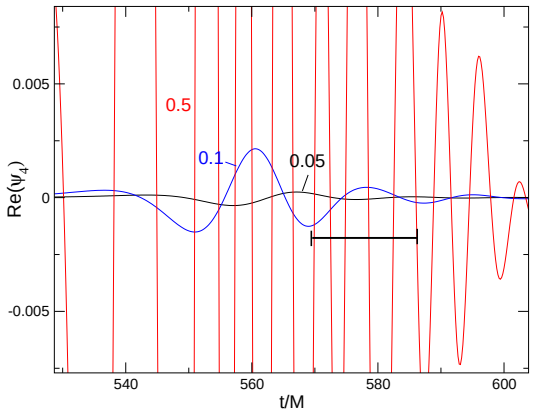


FIG. 11: Plunge and post-plunge radiation for models with $M\omega_{\rm LR}$ =0.05, 0.10, and 0.50. The radial fall is that of Fig. 10. The dark horizontal bar shows the period $\Delta t = 16.815\,M$ for a full wave of QNR. For $M\omega_{\rm LR} = 0.50$ the more rapid oscillations correspond approximately to the orbital frequency, not to the QN frequency.

question, we consider a family of trajectories, all with the radial motion used throughout this subsection ($\tau = 600$, $v_{\rm LR} = 0.3$) and all with $M\omega_{\rm LR} = 0.1$, a physically reasonable choice for which QNR is not dominated by direct radiation. We choose the models of Eq. (36) with $\sigma = 0$, 2, and -0.3. For these choices Fig. 12 shows that the time dependence of the orbital frequency differs significantly. The sensitivity to changes in the particle's orbital velocity can be inferred from the data in Fig. 11, where a change in $M\omega_{\rm LR}$ from 0.05 to 0.1 results in a sixfold increase in the amplitude of QNR. By that standard, these models should have quite different excitation of QNR if the particle angular velocity far from the LR were significant.

Figure 13 shows the computed plunge radiation (real part of the Teukolsky function) for the three models. Comparison of the amplitude of QNR cannot be made directly from plots of $\psi$ due to the phase differences in the radiation for the three models. We therefore apply the technique discussed at the beginning of this section, the technique of

"removing" the damping by multiplying by $\exp(0.088965\, t/M)$. The "undamped QNR," plotted in Fig. 13, shows the QNR as a series of oscillations of approximately constant amplitude. The appearance of this feature adds confidence that the radiation, during this epoch, is QNR, and it greatly narrows the uncertainty about where the QNR starts. Most important for our current concern, it also allows a direct comparison of the amplitudes for the different models.

From these results, with damping removed, we find that the QNR amplitudes for the $\sigma = -0.3$ model is roughly 15% greater than that of the $\sigma = 2$ or $\sigma = 0$ models. Some variation, of course, should be expected since it is not precisely the $\omega$ *at* the LR that is crucial, but rather the $\omega$ *near* the LR. Here "near" means within a e-damping time $\Delta t = M/0.0889 \approx 11M$. The variation in the models over that time makes it surprising that there is as little variation in QNR excitation as is computed; the principle that the LR motion is crucial is therefore strongly supported. The conclusion is yet stronger for physically correct models of geodesic motion, since those models have $d\omega/dt = 0$ at the LR.

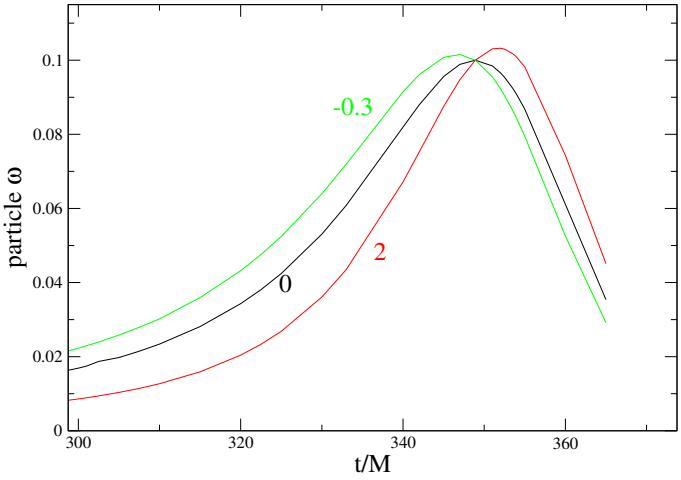


FIG. 12: Particle angular velocity as a function of time for models following Eq. (36) with $\omega_{\rm LR} = 0.1$, but with $\sigma = 0, 2, -0.3$. The $\sigma$ values are indicated in the plot.

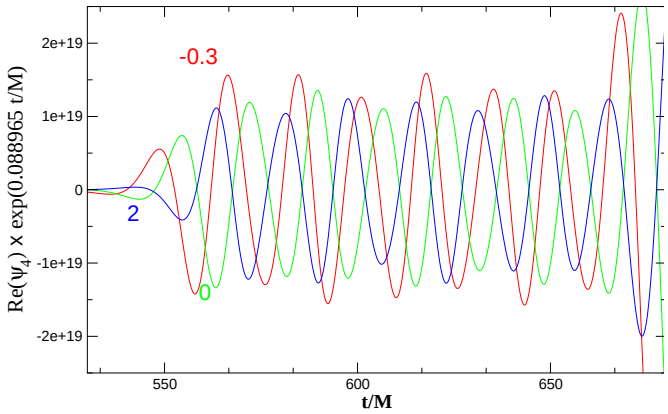


FIG. 13: The plunge radiation and QNR (real part of the Teukolsky function) for the infall models of this subsection. All curves here correspond to $\omega_{\rm LR} = 0.10$, but their orbital motion, as prescribed in Eq. (36), has different values of the $\sigma$ parameter, the values $\sigma = -0.3$, 0, and 2, as marked on the plot. Each curve has been multiplied by a factor $\exp(0.088965\, t/M)$ to remove the QN exponential decay. This greatly clarifies when QNR starts as well as facilitates the comparison of QNR with different phases.

### C. Direct radiation

Here we demonstrate that for orbital frequencies $\omega_{\rm LR}$ well above the frequency of Schwarzschild QNR, $M\omega = 0.37367$, the radiation is dominated by a field directly linked to the motion of the particle. With this we can infer that for frequencies near and somewhat larger than $M\omega = 0.37367$, the radiation will be a mixture of such direct radiation and QNR. We choose the specific case $M\omega_{\rm LR} = 4.0$, an order of magnitude above the frequency of QNR, a frequency at which we should see the direct radiation completely dominate the QNR.

To analyze the radiation at this high frequency we first need to deal with the fact that the orbital motion is so fast that many angular modes of radiation are generated and we lose the simplicity of a single multipole moment. For that reason, we present in Fig. 14 only the $\ell, m = 2, 2$ part of the radiation.

Several features of Fig. 14 are immediately interesting. The peak of the emission is around $t/M \approx 547$, the time at which the retarded location of the particle orbit is at the $r = 3M$ location of the LR. The "edge" of the curvature potential in the Schwarzschild spacetime is, of course, not a sharp well defined edge as in the TDP, so the LR is only a nominal representation of an edge location. A second point to notice is that the increasing amplitude for $t/M \lesssim 547$ can be ascribed to the increasing particle acceleration, and the decreasing amplitude for $t/M \gtrsim 547$, can be understood as a redshift effect.

To delve more deeply into the nature of the "direct" radiation in Fig. 14 we plot, in Fig. 15, a comparison of the frequency exhibited by the computed wave (inferred from the spacing between the zeros of the waveform) and the frequency that one expects for radiation coming directly from the particle's orbital motion. This expected frequency is computed by noting, for a particular "emission time" in the particle's trajectory, the angular frequency of the particle as given by Eq. (36). The "observation time" is then computed for the radiation from this event to reach the wave extraction radius $r^* = 200M$; it is this observation time that is the horizontal axis in Fig. 15. The frequency is then multiplied by two to account for the fact that the gravitational waves are $m = 2$. Lastly, the Doppler shift of the outgoing radiation is taken into account by dividing the frequency by $1 + v$, where $v$ is the ingoing radial speed of the particle at the emission time. The excellent agreement between this prediction and the waveform observed leaves no doubt that this is "direct" radiation, and unrelated to the relatively low quasinormal frequency (indicated in the plot by a short horizontal line).

The analysis of direct radiation may turn out to be more than a useful check on consistency; it may turn out to be an interesting diagnostic in the Kerr spacetime. In the Schwarzschild spacetime, the amplitude vs. frequency result has, embedded in it, information about the way in which the curvature potential acts as a high pass filter for radiation passing outward. It has been suggested[33] that amplitude vs. frequency curves may lead to an effective Kerr curvature potential.

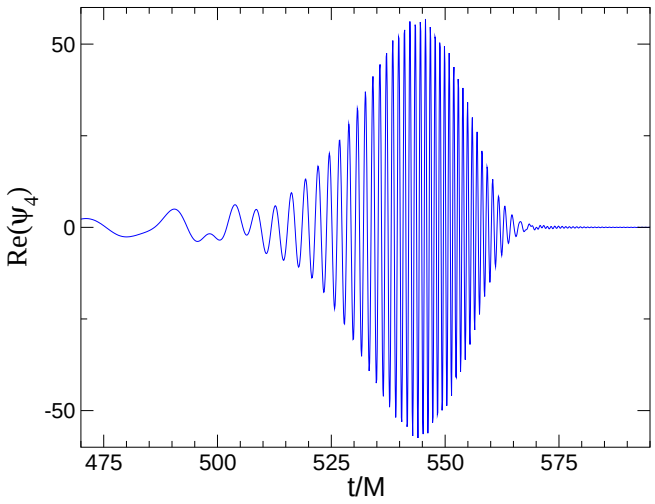


FIG. 14: The real part of the Teukolsky function for our infall model with $\omega_{\rm LR} = 4$. The $\ell, m = 2, 2$ part of the solution is presented.

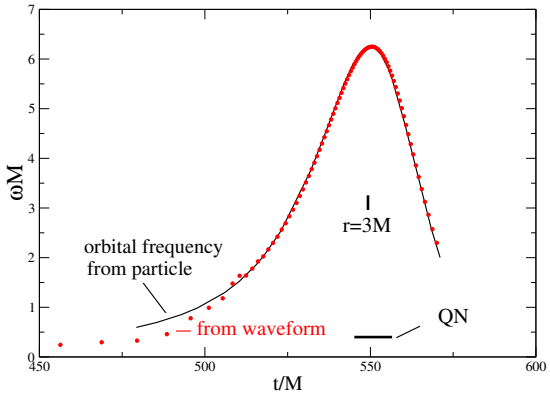


FIG. 15: A comparison of the frequency seen in the evolved waveform (circles) and the frequency inferred from the particle motion (solid curve). The waveform results above $t \approx 570$ are noisy due to the small amplitude of the computed waves. Five-point averaging was applied to smooth the waveform results below $t \approx 515$. The horizontal bar shows the value of a period corresponding to the frequency $\omega M = 0.37367$ for the least damped QN quadrupole mode. See text for details of the computation of the frequency inferred from the particle motion.

## VI. DISCUSSION

Though great attention has been given to the connection of QN frequencies and the LR[9–14], much less has been given to the question of why the LR should play such a crucial role in the generation of plunge radiation and the *excitation* of QNR? From the point of view of multipole decomposition and the curvature potential, this is because the curvature potential takes a simple flat spacetime multipole form for $r \gg 3M$, and is negligibly small far on the other side of the LR (more precisely for $1 - 2M/r \ll 1$). But this observation is not an explanation. An explanation must be rooted in the physical process being described before multipoles are projected.

That physical process is the generation of disturbances by the motion of a particle. Disturbances propagate along characteristics, the same world lines as the paths of photons. Consider a particle and an observer both far outside ($r \gg 3M$) a black hole. Disturbances (scalar or whatever) of the particle will travel on the usual characteristics connecting the moving particle to the observer. Due to the presence of the black hole, however, there will be extra, non-flat-spacetime characteristics connecting the particle and observer. These will correspond to zoom-whirl orbits that go around the black hole, just outside the LR, and end up at the particle. Though interesting as a matter of principle, these extra "nonstandard" characteristics will play little role if the black hole is far away; the cross section for such characteristics will be too small.

When the particle is close to the LR, however, the effect of the zoom-whirl characteristics will be dramatic. These "extra" characteristics will dominate over the standard characteristics as the particle passes through the LR. It is expected, and confirmed by studies of trajectories, that as the particle proceeds inward, its characteristics more and more lose the ability to reach the external observer and the particle and observer become more and more causally disconnected. This picture of the zoom-whirl characteristics give a fairly persuasive heuristic argument that radiation that will be characteristic of the black hole, plunge radiation and QNR, must come from the region of the LR.

## VII. CONCLUSION

In this paper we have used the Fourier domain Green function to understand why the excitation of plunge radiation and quasinormal ringing might be determined by source conditions at the light ring of a black hole. We then verified that hypothesis of light ring cruciality with models both using Green function computations and numerical evolution. A particular insight informed by both methods was that the plunge radiation and quasinormal ringing, at least in the case of radial infall, can be primarily ascribed to the particle motion after crossing the light ring.

Such insights can be viewed as a successful first step in understanding the plunge/ringing phase of binary black hole inspiral/merger, but only the first step. In particular, this work has relied on the particle perturbation linearization of general relativity. There are good reasons to believe that the lessons from that simplification apply to the binary motion of comparable mass holes, but this needs to be investigated.

It will be necessary to extend our study to rotating holes, an extension which will be particularly interesting since there are two distinct light rings in the equatorial plane, one for prograde photon orbits and one for retrograde orbits,

and there are light rings for a continuum of radii if nonequatorial orbits are considered. Work on this analysis is already underway.

### Acknowledgments

We thank Scott Hughes of MIT and Alessandra Buonanno, of the Max Planck Institute for Gravitational Physics, for very useful discussions of several aspects of this work. We express sincere and profound thanks to two exceptionally conscientious referees whose careful reading of the original version of this paper have led to a much clearer and less error-prone presentation. SN acknowledges support from the Center for Gravitational Wave Astronomy at UTB. GK acknowledges research support from NSF Grant Nos. PHY-1303724, PHY-1414440 and from the U.S. Air Force agreement No. 10-RI-CRADA-09.

## Appendix A: Fourier Domain Green Function for the TDP

### 1. Method

We give here the details of the FDGF for the simple TDP model. The method is to find a solution of Eq. (10) for the potential in Eq. (12). The model is simple because the homogeneous solutions of Eq. (10) are the elementary functions

$$\mathcal{G} \propto \begin{cases} e^{i\omega x},\ e^{-i\omega x} & \text{for } x < x_0 \\ e^{i\omega x}\left(1 + i/(\omega x)\right),\ e^{-i\omega x}\left(1 - i/(\omega x)\right) & \text{for } x > x_0 \end{cases} . \tag{A1}$$

A solution for $\mathcal{G}$ is constructed by imposing outgoing boundary conditions ($\mathcal{G} \propto e^{i\omega x}\left(1 + i/\omega x\right)$) for $x > \max(a, x_0)$, and ingoing boundary conditions ($\mathcal{G} \propto e^{-i\omega x}$) for $x < \min(a, x_0)$. The values of $x, x_0$ and $a$ then separate the solution into three forms with four coefficients. The coefficients are determined by requiring that the solution be continuous everywhere and have a unit discontinuity in its derivative at $x = a$.

The form of the solution depends on the order of $x, x_0$ and $a$, and the presentation of the solution is separated accordingly. We also present the results for $\Psi$, using these FDGFs, for radial infall with $f(t) = 1$.

### 2. Solutions for $x > a > x_0$.

In this case the FDGF

$$\mathcal{G} = \frac{e^{i\omega(x-a)}e^{-2i\omega x_0}\left((1+ia\omega)e^{2i\omega x_0}\left(2\omega^2{x_0}^2 + 2i\omega x_0 - 1\right) + e^{2ia\omega}(1 - ia\omega)\right)}{2a\omega^2\left(2\omega^2{x_0}^2 + 2i\omega x_0 - 1\right)}\left(1 + \frac{i}{x\omega}\right) .$$

A convenient rearrangement is

$$\mathcal{G} = -\,e^{-i\omega(-x+a)}\left(\frac{1}{2i\omega} - \frac{1}{2a\omega^2} + \frac{1}{2x\omega^2} - \frac{i}{2ax\omega^3}\right)$$

$$-\,\frac{e^{-i\omega(-x-a+2x_0)}}{2x_0^2(\omega-\omega_1)(\omega-\omega_2)}\left(\frac{1}{2i\omega} + \frac{1}{2a\omega^2} + \frac{1}{2x\omega^2} + \frac{i}{2ax\omega^3}\right) . \tag{A2}$$

Now we define the following two special particle times $T_1$ and $T_2$ as

$$T_1 = t - x + F(T_1) \qquad T_2 = t - x + 2x_0 - F(T_2)\,. \tag{A3}$$

The meaning of these two particle times is illustrated in the spacetime cartoon in Fig. 16.

With these definitions, and with Eq. (11), we get the following:

$$\Psi(t,x) = -\,\frac{1}{2}\int_{-\infty}^{T_1}\left[1 + \left(\frac{1}{x} - \frac{1}{a}\right)(t - T - x + a) - \frac{(t - T - x + a)^2}{2ax}\right] dT$$

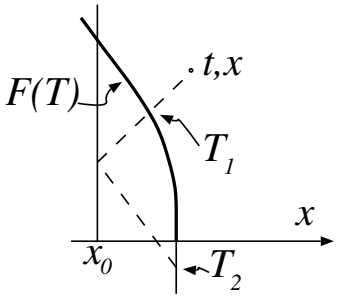


FIG. 16: A spacetime diagram showing the meaning of $T_1$ and $T_2$. The bold line represents the trajectory of the particle $x = F(T)$; the dashed lines are radial characteristics.

$$-\frac{1}{2}\int_{-\infty}^{T_2}\left[1+\left(\frac{1}{a}+\frac{1}{x}\right)(t-T-x-a)+\frac{(t-T-x-a)^2}{2ax}\right]dT$$

$$-\frac{1}{2}\int_{-\infty}^{T_2}e^{-\xi}\left[-(\cos\xi+\sin\xi)+2x_0\left(\frac{1}{a}+\frac{1}{x}\right)\cos\xi-\frac{2x_0^2}{ax}(\cos\xi-\sin\xi)\right]dT\,. \tag{A4}$$

Here $\xi$ is

$$\xi=(t-T-x-a+2x_0)/2x_0\,. \tag{A5}$$

The first two integrals in Eq. (A4) can be combined so that the result is in manifestly finite form,

$$\Psi(t,x)=-\frac{1}{2}\int_{T_2}^{T_1}\left[1+\left(\frac{1}{x}-\frac{1}{a}\right)(t-T-x+a)-\frac{(t-T-x+a)^2}{2ax}\right]dT$$

$$-\frac{1}{2}\int_{-\infty}^{T_2}e^{-\xi}\left[-(\cos\xi+\sin\xi)+2x_0\left(\frac{1}{a}+\frac{1}{x}\right)\cos\xi-\frac{2x_0^2}{ax}(\cos\xi-\sin\xi)\right]dT\,. \tag{A6}$$

Note that this solution is good only for $u\equiv t-x$ less than or equal to the value of $u$ corresponding to $u_{\rm crit}=T_{\rm cross}-x_0$, where $T_{\rm cross}$ is the time at which the particle reaches $x_0$. For larger values of $u$ the Green function for $a>x_0$ is no longer valid.

### 3. Solution for inner region $x<x_0<a$

In this case the FDGF is

$$\mathcal{G}=\frac{e^{i\omega(a-x)}(1-ia\omega)}{2a(\omega-\omega_1)(\omega-\omega_2)}\,. \tag{A7}$$

so that

$$\Psi=\frac{1}{2\pi}\int_{-\infty}^{\infty}\int_{-\infty}^{\infty}\frac{e^{-i\omega(t-T-a+x)}(1-ia\omega)}{2a(\omega-\omega_1)(\omega-\omega_2)}\,dTd\omega$$

We now define $T_3$ by $t+x=T_3+F(T_3)$, as illustrated in Fig. 17, and we define

$$\sigma\equiv(t-T+x-a)/2x_0.$$

With these we get

$$\Psi=-\frac{x_0}{a}\int_{-\infty}^{T_3}e^{-\sigma}\left[\left(1-\frac{a}{2x_0}\right)\sin\sigma+\frac{a}{2x_0}\cos\sigma\right]dT\,. \tag{A8}$$

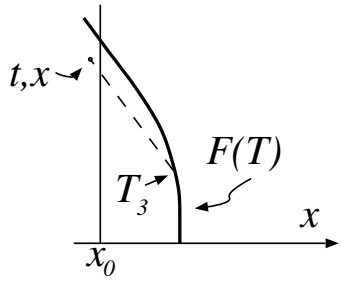


FIG. 17: A spacetime diagram showing the meaning of $T_3$. The bold line represents the trajectory of the particle $x = F(T)$; the dashed line is an ingoing radial characteristic.

### 4. Solution for intermediate region $x_0 < x < a$

Here the FDGF is

$$\mathcal{G} = \frac{e^{-i\omega(x-a)}(1-ia\omega)}{2a\omega^2}\left(1-\frac{i}{\omega x}\right) - \frac{e^{-i\omega(-x-a+2x_0)}(1-ia\omega)}{4a\omega^2 x_0^2(\omega-\omega_1)(\omega-\omega_2)}\left(1+\frac{i}{\omega x}\right). \tag{A9}$$

We define $T_4$ and $T_5$ by

$$T_4 + F(T_4) = t + x \qquad T_5 + F(T_5) = t - x + 2x_0\,. \tag{A10}$$

and illustrate them in Fig. 18.

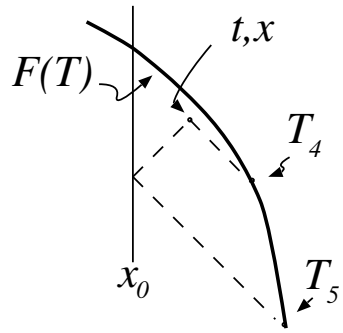


FIG. 18: A spacetime diagram showing the meaning of $T_4$ and $T_5$. The bold line represents the trajectory of the particle $x = F(T)$; the dashed lines are radial characteristics.

For evaluation of the integrals leading to $\Psi$ it is convenient to define

$$K_4 \equiv t - T + x - a \qquad K_5 \equiv t - T - x - a + 2x_0 \qquad \varepsilon \equiv K_5/2x_0\,. \tag{A11}$$

We now break up the integral for $\Psi$ into three parts and write $\Psi = I_1 + I_2 + I_3$, where

$$I_1 = \frac{1}{2a}\int_{-\infty}^{T_4}\left[-a - \left(1-\frac{a}{x}\right)K_4 + \frac{1}{2x}K_4^2\right]dT \tag{A12}$$

$$I_2 = \frac{1}{2a}\int_{-\infty}^{T_5}\left[-a + \left(1+\frac{a}{x}\right)(-K_5+2x_0) - \frac{1}{2x}\left(K_5^2 - 4x_0K_5 + 4x_0^2\right)\right]dT \tag{A13}$$

$$I_3 = \frac{1}{2}\int_{-\infty}^{T_5} e^{-\varepsilon}\left[\cos\varepsilon + \sin\varepsilon - 2x_0\left(\frac{1}{a}+\frac{1}{x}\right)\cos\varepsilon + \frac{2x_0^2}{ax}\left(\cos\varepsilon - \sin\varepsilon\right)\right]dT\,. \tag{A14}$$

We can combine $I_1$ and $I_2$ to give an answer that is manifestly finite

$$\Psi = \frac{1}{2a}\int_{T_5}^{T_4}\left[-a-\left(1-\frac{a}{x}\right)K_4+\frac{1}{2x}K_4^2\right]\,dT$$

$$+\frac{1}{2}\int_{-\infty}^{T_5} e^{-\varepsilon}\left[\cos\varepsilon+\sin\varepsilon-2x_0\left(\frac{1}{a}+\frac{1}{x}\right)\cos\varepsilon+\frac{2x_0^2}{ax}\left(\cos\varepsilon-\sin\varepsilon\right)\right]\,dT\,. \tag{A15}$$

### 5. Static solution for $a > x_0$

For comparison with evolution codes, it is important to know the initial data for evolution. This follows from setting $\omega = 0$ in Eq. (10) and using the potential in Eq. (12). The static solution must have the form

$$\Psi = \begin{cases} \alpha/x & \text{for } x > a \\ \beta/x + \xi x^2 & \text{for } x_0 < x < a \\ \delta & \text{for } x < x_0 \end{cases}\,. \tag{A16}$$

When the coefficients are matched at $x = a$ and $x = x_0$, so that the solutions are continuous everywhere and have a unit jump in their derivative at $x = a$, the coefficients are found to be

$$\alpha = -a^2/3 - 2x_0^3/3a \qquad \beta = -2x_0^3/3a \qquad \gamma = -1/3a \qquad \delta = -x_0^2/a\,. \tag{A17}$$

### 6. Solutions for $a < x_0 < x$

Here the FDGF is

$$\mathcal{G} = -\frac{i}{2}\frac{e^{-i\omega(a-x)}\omega}{(\omega-\omega_1)(\omega-\omega_2)}\left(1+\frac{i}{\omega x}\right)\,. \tag{A18}$$

We define $T_6$ and $\theta$ by

$$T_6 - F(T_6) = t - x \qquad \theta = (t - T + a - x)/2x_0\,, \tag{A19}$$

and illustrate them in Fig. 19.

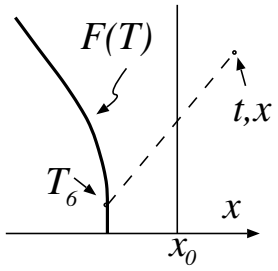


FIG. 19: A spacetime diagram showing the meaning of $T_6$. The bold line represents the trajectory $x = F(T)$ of the particle; the dashed line represents a radial characteristic.

If the particle has always been moving in the $a < x_0$ region, then the Green function gives the solution

$$\Psi = \frac{x_0}{2}\int_{-\infty}^{T_6} e^{-\theta}\left[\frac{1}{x_0}\left(\sin\theta-\cos\theta\right)-\frac{2}{x}\sin\theta\right]\,dT\,. \tag{A20}$$

In the case that mainly interests us, the particle will start at a position greater than $x_0$ and cross $x_0$ at some time $T_{\rm cross}$. We will need to calculate $\Psi$ for values of retarded time $u$ both less than and greater than $u_{\rm crit} = T_{\rm cross} - x_0$. For $u < u_{\rm crit}$ we find $\Psi$ from Eq. (A6). For $u > u_{\rm crit}$ we need Eq. (A20), but the lower limit of integration must be

changed from $-\infty$, to $T_{\rm cross}$, since the $a < x_0$ Green function only applies for $T > T_{\rm cross}$. To this integral must be added the contributions for $T < T_{\rm cross}$. This comes from Eq. (A6) adapted to $u > u_{\rm crit}$.

To understand how to adapt Eq. (A6), note that when $u = u_{\rm crit}$ both $T_1$ and $T_2$ are equal to $T_{\rm cross}$. Thus for $u > u_{\rm crit}$, the case we are interested in here, both $T_1$ and $T_2$ are greater than $T_{\rm cross}$. But the integration over this range of $T$ must not exceed $T = T_{\rm cross}$, since here the Green function is only applicable when $F(T) > x_0$. Thus, both $T_1$ and $T_2$ must be replaced by $T_{\rm cross}$ in Eq. (A6). With this change, the first integral is missing from Eq. (A6) and the second integration extends only to $T_{\rm cross}$. The complete expression then is

$$\Psi = \frac{x_0}{2}\int_{T_{\rm cross}}^{T_6} e^{-\theta}\left[\frac{1}{x_0}\left(\sin\theta - \cos\theta\right) - \frac{2}{x}\sin\theta\right] dT$$

$$-\frac{1}{2}\int_{-\infty}^{T_{\rm cross}} e^{-\gamma}\left[-(\cos\gamma + \sin\gamma) + 2x_0\left(\frac{1}{a}+\frac{1}{x}\right)\cos\gamma - \frac{2x_0^2}{ax}\left(\cos\gamma - \sin\gamma\right)\right] dT\,. \tag{A21}$$

In the first integral, representing the contribution after the particle has passed inward through $x_0$, the definition of $T_6$ and $\theta$ are, as before, those given in Eq. (A19). In the second integral, representing the contribution before the particle has crossed, the definitions of $\gamma$ is the same as that given for $\xi$ in Eq. (A5).

### 7. Solution for innner region $x < a$

Here the Green function is

$$\mathcal{G} = -\frac{i}{2\omega}\,e^{-i\omega(x-a)} + \frac{i}{2\omega}\,e^{-i\omega(x+a-2x_0)} + \frac{e^{-i\omega(x+a-2x_0)}}{2x_0(\omega-\omega_1)(\omega-\omega_2)}\,. \tag{A22}$$

We define $T_7$ and $T_8$ as follows, and illustrate them in Fig. 20,

$$T_7 + F(T_7) = t + x \qquad T_8 - F(T_8) = t + x - 2x_0\,. \tag{A23}$$

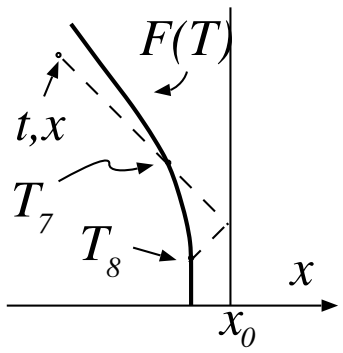


FIG. 20: A spacetime diagram showing the meaning of $T_7$ and $T_8$. The bold line represents the trajectory of the particle $x = F(T)$; the dashed lines are radial characteristics.

With $\varphi$ defined as

$$\varphi = (t - T + x + a - 2x_0)/2x_0\,, \tag{A24}$$

the solution for $\Psi$ becomes

$$\Psi = -\frac{1}{2}\int_{T_8}^{T_7} dt - \int_{-\infty}^{T_8} e^{-\phi}\sin\phi dT\,. \tag{A25}$$

### 8. Solution for intermediate region $x_0 > x > a$

Here the Green function is

$$\mathcal{G} = -\,i\frac{e^{-i\omega(a-x)}}{2\omega} - \,i\frac{e^{-i\omega(x+a-2x_0)}}{4\omega x_0^2(\omega-\omega_1)(\omega-\omega_2)}\,. \tag{A26}$$

We now define $\varphi$ and the times $T_9$, $T_{10}$ illustrated in Fig. 21.

$$T_9 - F(T_9) = t - x \qquad T_{10} - F(T_{10}) = t + x - 2x_0 \qquad \varphi = (t - T + x + a - 2x_0)/2x_0\,. \tag{A27}$$

With these we arrive at

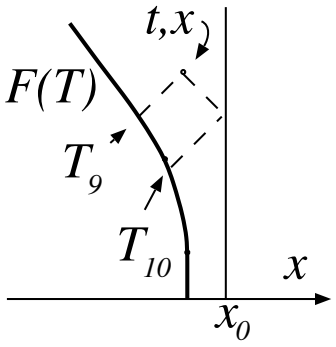


FIG. 21: A spacetime diagram showing the meaning of $T_9$ and $T_{10}$. The bold line represents the trajectory of the particle $x = F(T)$; the dashed lines are radial characteristics.

$$\Psi = -\,\frac{1}{2}\int_{T_{10}}^{T_9} dT - \frac{1}{2}\int_{-\infty}^{T_{10}} e^{-\varphi}\,(\cos\varphi + \sin\varphi)\;dT\,. \tag{A28}$$

### 9. Static solution for $a < x_0$

Let a unit particle be stationary at $x = a < x_0$. We decompose the static solution as follows:

$$\Psi = \begin{cases} \alpha/x & \text{for } x > x_0 \\ \beta + \gamma x & \text{for } a < x < x_0 \\ \delta & \text{for } x < a \end{cases}\,. \tag{A29}$$

The conditions at $x = x_0$ are continuity and smoothness; the conditions at $x = a$ are continuity and a unit jump in $d\Psi/dx$. The solutions are easily found to be

$$\Psi = \begin{cases} -x_0^2/x & \text{for } x > x_0 \\ -2x_0 + x & \text{for } a < x < x_0 \\ -2x_0 + a & \text{for } x < a \end{cases}\,. \tag{A30}$$

[1] L. Lehner, F. Pretorius, Annual Review of Astronomy and Astrophysics, 52, 661 (2014).
[2] V. Cardoso, L. Gualtieri, C. Herdeiro, U. Sperhake, Living Rev. Relativity, 18, 1 (2015).
[3] L. L. Smarr, Ph.D. dissertation, University of Texas at Austin, unpublished (1975); K. R. Eppley, Ph.D. dissertation, Princeton University, unpublished (1977); L. L. Smarr, in *Sources of Gravitational Radiation*, Cambridge University Press (1979).
[4] C. M. Will, *Theory and Experiment in Gravitational Physics*, Cambridge University Press (1993); E. Poisson and C. M. Will, *Gravity: Newtonian, Post-Newtonian, Relativistic*, Cambridge University Press (2014).
[5] C. V. Vishveshwara, Phys. Rev. D 1, 2870 (1970); W. H. Press, Astrophys. J. 170, L105 (1971); S. Chandrasekhar and S. L. Detweiler, Proc. R. Soc. Lond. A 344, 441 (1975); S. Chandrasekhar, *The Mathematical Theory of Black Holes*, Oxford University Press (1998).
[6] The importance of the plunge epoch is clear in any of the many examples of complete binary waveforms that have been published. See, for example, T. W. Baumgarte and S. Shapiro, Physics Today **64**, 32 (2011).
[7] F. Pretorius, Phys. Rev. Lett. 95, 121101 (2005); M. Campanelli, C. O. Lousto, P. Marronetti and Y. Zlochower, Phys. Rev. Lett. 96, 111101 (2006); J. G. Baker, J. Centrella, D. I. Choi, M. Koppitz and J. van Meter, Phys. Rev. Lett. 96, 111102 (2006); T. W. Baumgarte and S. L. Shapiro, *Numerical Relativity*, Cambridge University Press, (2010); L. Lehner and F. Pretorius, Annual Review of Astronomy and Astrophysics 52, 661 (2014).
[8] T. Damour and A. Gopakumar, Phys. Rev. D **73**, 124006 (2006).
[9] C. J. Goebel, Astrophys. J. Letters, **172** L95-96 (1972).
[10] V. Ferrari, and B. Mashhoon, Phys. Rev. D **30**, 295 (1984)
[11] A. Buonanno, G. B. Cook, F. Pretorius, Phys. Rev. D 75, 124018 (2007).
[12] E. Berti, V. Cardoso, J. A. Gonzalez, U. Sperhake, M. Hannam, S. Husa, B, Bruegmann, Phys. Rev. D 76, 064034 (2007).
[13] H. Yang, D. A. Nichols, F. Zhang, A. Zimmerman, Z. Zhang, Y. Chen, Phys. Rev. D 86, 104006 (2012).
[14] S. R. Dolan, A. C. Ottewill, Phys. Rev. D 84, 104002 (2011).
[15] A. Taracchini, A. Buonanno, G. Khanna, S. A. Hughes, Phys. Rev. D**90**, 084025 (2014); E. Barausse, A. Buonanno, S. A. Hughes, G. Khanna, S. O'Sullivan, Y. Pan, Phys. Rev. D**85**, 024046 (2012).
[16] C. W. Misner, K. S. Thorne, and J. A. Wheeler, *Gravitation* (W. H. Freeman, San Francisco, 1973).
[17] C. O. Lousto, H. Nakano, Y. Zlochower, M. Campanelli, Phys. Rev. D 82, 104057 (2010).
[18] U. Sperhake, V. Cardoso, C. D. Ott, E. Schnetter, H. Witek, Phys. Rev. D 84, 084038 (2011).
[19] E. Berti, V. Cardoso, T. Hinderer, M. Lemos, F. Pretorius, U. Sperhake, N. Yunes, Phys. Rev. D 81, 104048 (2010).
[20] H. Nakano, Y. Zlochower, C. O. Lousto, Campanelli, Phys. Rev. D 84, 124006 (2011).
[21] R. H. Price, G. Khanna, and S. A. Hughes, Phys. Rev. D **83**, 124002 (2011).
[22] R. H. Price, G. Khanna, and S. A. Hughes, Phys. Rev. D **88**, 104004 (2013).
[23] J. D. Schnittman, A. Buonanno, J. R. van Meter, J. G. Baker, W. D. Boggs, J. Centrella, B. J. Kelly, and S. T. McWilliams, Phys. Rev. D **77**, 044031 (2008).
[24] P. A. Sundararajan, G. Khanna, and S. A. Hughes, Phys. Rev. D **81**, 104009 (2010).
[25] T. Regge and J.A. Wheeler, Phys. Rev. **108**, 1063 (1957).
[26] Various authors use different names ("effective potential," "scattering potential, "curvature potential") for this potential-like term. See, e.g., W. H. Press, Astrophys. J. 170, L105 (1971); R. H. Price, Phys. Rev. D 5, 2419 (1972); A. Buonanno, AIP Conference Proceedings 968, 307 (2008); F. J. Zerilli, Phys. Rev. Lett. **24**, 737 (1970).
[27] The curvature potential can also depend on the mathematical representation of the perturbation. For example, the potentials in the wave equation of Zerilli *op cit.*, and the Bardeen-Press equation (J. M. Bardeen, W. H. Press, J. Math. Phys. **14**, 7 (1973)) describe the same physical perturbations, but have different curvature potentials.
[28] E. W. Leaver, J. Math. Phys. **27**, 1238 (1986).
[29] Price, R. H., Phys. Rev. D **5**, 2419 (1972); H.-P. Nollert, Classical and Quantum Gravity **16**, 159 (1999).
[30] Quasinormal frequencies for Truncated multipole potentials are given by S. Chardrasekhar and S. Detweiler, Royals Society of London Proceedings Series A **344**, 441-452 (1975). In this paper the potential is called "Price's potential," and the results for QN frequencies are attributed to W. Press in unpublished work. For a discussion of the truncated quadrupole potential see S. Nampalliwar, Ph.D. thesis, University of Texas at Brownsville, 2015.
[31] The plots seem to suggest that QNR excitation increases with increasing $v_{\rm cross}$, contrary to earlier arguments. Note that the early large negative dip in the plots is *not* QNR. The true correlation of $v_{\rm cross}$ and QNR can be verified by using the technique demonstrated in Fig. 13. Here that means multiplying the curves by $\exp(.5t)$ in order to identify the onset and amplitude of QNR. This technique shows that indeed QNR decreases with increasing $v_{\rm cross}$.
[32] L. M. Burko, G. Khanna, Europhys. Lett. 78, 60005 (2007); P. A. Sundararajan, G. Khanna, S. A. Hughes, Phys. Rev. D 76, 104005 (2007); P. A. Sundararajan, G. Khanna, S. A. Hughes, S. Drasco, Phys. Rev. D 78, 024022 (2008); P. A. Sundararajan, G. Khanna, S. A. Hughes, Phys. Rev. D 81, 104009 (2010); J. McKennon, G. Forrester, G. Khanna, Proceedings of the NSF XSEDE12 Conference, Chicago, IL (2012).
[33] Alessandra Buonanno, private communication.